Journal of Applied Fluid Mechanics, Vol. 18, No. 1, pp. 191-204, 2025.
Available online at www.jafmonline.net, ISSN 1735-3572, EISSN 1735-3645.
https://doi.org/10.47176/jafm.18.1.2737

Effect of Solidity and Camber Angle on Performance in Contra-rotating Open Rotor Design

Q. Wang [1], L. Zhou [1,2†] and Z. Wang [1]

[1] *School of Power and Energy, Northwestern Polytechnical University, Xi'an Shaanxi,710129, China*
[2] *Innovation Center for Advanced Aero-Engine, Beijing,100191, China*

†*Corresponding Author Email: zhouli@nwpu.edu.cn*

ABSTRACT

In this paper, an aerodynamic design method for a contra-rotating open rotor based on lifting line theory is presented. By changing the number of blades, the solidity and camber angle are changed, and several different aerodynamic designs are completed. The effect of solidity and camber angle on the aerodynamic performance is studied. The results show that when the number of blades increases, the solidity linearly increases while the camber angle nonlinearly decreases. There exists an optimal number of blades for aerodynamic design. The highest propulsion efficiency improved by 2.41% compared to the lowest value. The highest propulsion efficiency of 0.81 occurred with 10 blades. Increased solidity leads to increased viscous and wake losses. The change in solidity also changes the shock wave structure in the channel and the static pressure distribution on the blade surface. When the number of blades is reduced, decreased solidity results in greater circumferential differential pressure. The increased camber angle brings a larger inverse pressure gradient in the flow direction. This resulted in a significant flow reversal region in the channel, increasing the rear rotor root losses.

Article History

Received March 17, 2024
Revised June 30, 2024
Accepted August 3, 2024
Available online November 6, 2024

Keywords:

Aerodynamic design
Solidity
Camber angle
Shock wave structure
Flow reversal region

1. INTRODUCTION

The contra-rotating open rotor (CROR) engine has the advantage of high propulsion efficiency, making it one of options the next generation of civil aircraft (Perullo et al., 2013; Busch et al., 2015). Compared to conventional turbofan engines, such as the CFM56, the CROR concept holds the promise of up to 30% fuel burn reduction (Brouckaert et al., 2018).

The geometric and flow characteristics of the CROR are between those of the propeller (Wald, 2006; Liu et al., 2016,) and fan (Kuang et al., 2017, Sun et al., 2017). Compared with the traditional propeller, the CROR has more blades with a significant aft-sweep feature (Kirker, 1990). In addition, the flight Mach number is higher. Compared with the fan, the CROR has fewer blades. Because there is no limitation in this case, the rotor diameter is larger and the solidity is smaller.

Depending on the flow characteristics of the CROR, the design can be completed based on a fan or propeller design method with modifications, or a combination of these two design approaches.

When the fan design method is used, it is critical to modify the impact of the absence of the case. Smith (1987) used the compressor design method for the CROR design. The effect of not having a case was considered by introducing a secondary flow at the blade tip. The research team of GE36 (GE36 Design and Systems Engineering, 1987) used wall boundaries away from the rotor flow field during the design process to simulate the effect of having no case. Ten percent of the total flow was allowed to pass through the blades.

Some researchers have used propeller design approaches. Playle et al. (1986) designed a CROR and predicted the off-design-point performance based on Theodorsen's theory, and introduced airfoil data. Hanson (1983) utilized the compressible helicoidal surface theory for the aerodynamic and noise design of rotors. Barry et al. (2014) conducted research on the open-rotor installation performance using the Reynolds-averaged lifting-line method. Nigam et al. (2015) developed the AERO-AP design software based on the open source XROTOR code using discrete vortex equations, and optimized the design using a genetic algorithm. Zhou and Shan (2017) carried out a single-row propfan design based on the compressible lifting surface theory, which strictly deals with rotor

NOMENCLATURE

Parameters

A	annular Area
b	chord length
c	absolute velocity
$C_T = \frac{T}{\rho n^2 D^4}$	thrust coefficient
$C_P = \frac{P}{\rho n^3 D^5}$	power coefficient
$C_p = \frac{p - p_0}{\frac{1}{2}\rho_\infty v_\infty^{\ 2}}$	static pressure coefficient
D	diameter of the rotor
$\tilde{f}$	maximum camber position
H	Lagrange multiplier method
J	advance ratio
n	rotation speed
p	static pressure
p^*	absolute total pressure
P	shaft power
PQA	total power coefficient
Q	torque
R_{tip}	radius of the rotor
R_{hub}	radius of the hub
T	thrust
T_{required}	required thrust
T_P	axial component of the pressure force
T_μ	axial component of the viscous force
t	blade pitch
v_s	ship speed
v_Z	axial velocity
w	relative velocity
Z	blade number

Greek symbols

β	Stagger angle
Γ	Circulation
γ	Gas constant
λ	Lagrange multiplier
η_{P}	Propulsion efficiency
η_{R}	isentropic efficiency
π	static pressure ratio
θ	camber angle
ρ	density
τ	solidity
ω	rotation speed

Subscripts

f	front rotor
r	rear rotor
u	circumferential component
0	ambient
1	front inlet
2	front outlet
3	rear inlet
4	rear outlet
∞	far field

Abbreviations

CFD	Computational Fluid Dynamics
CROR	Contra-Rotating Open Rotor
LE	Leading Edge
PS	Pressure Surface
SS	Suction Surface
TE	Trailing Edge

rotation, flow compressibility, wide chord and large aft-swept blades, and blade interaction under the small distribution linearization assumption in a rotating coordinate system.

Some researchers have also used both fan and propeller design methods. Rohrbach (1976) and Black et al. (1978) segmented the blades. A compressor design method was used for blade roots with high solidity. The propeller design method was used to design the middle and upper parts of a blade with low solidity. Compressible airfoil data was introduced to modify the effect of a high Mach number.

As the main thrust-generating component, the aerodynamic design of a CROR is performed to obtain the required thrust based on a given Mach number and flight altitude, and its propulsion efficiency is sufficiently high under cruise conditions (Larsson et al., 2014). The values of the remaining parameters have some freedom of selection. Complex flow phenomena exist in axial-flow turbomachinery (Stürmer et al., 2012; Kan et al., 2021a), and design space needs to be considered (Van Zante et al., 2014; Kan et al., 2021b). These parameters are classified into two categories. The first includes overall design parameters such as rotational speed, diameter, and hub ratio. The second includes geometric parameters such as solidity, camber angle, and stagger angle (Stuermer, 2008). Constraints exist between these two types of parameters (Aungier, 2003). Besides, constraints exist between the geometric parameters. Therefore, during the design, overall design parameters' change will be delivered to the geometric parameters, resulting in significant changes in the aerodynamic performance. Thus, the correct selection of the values of the design parameters is very important for realizing the high propulsion efficiency.

The solidity and camber angle, which are important geometric parameters of axial-flow turbomachinery (Britsch et al., 1979), have been shown to greatly affect the flow field and the blade load in earlier studies of compressors and cascades. In the aerodynamic design of the CROR, owing to the small number of blades, changes in the blade number significantly change the solidity and single-blade load, which affects the design results.

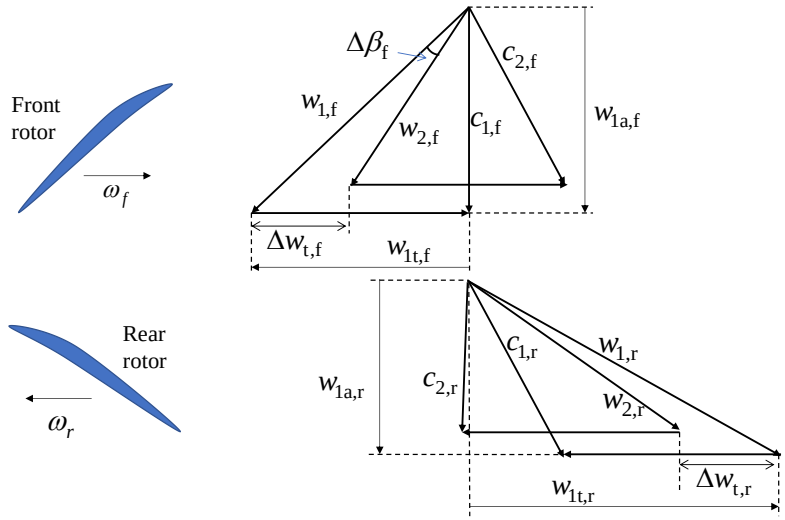

Fig. 1 Velocity triangle of CROR

Therefore, it is necessary to design CRORs with different blades to explore the relationship between the number of blades, solidity, and camber angle. The effects of the solidity and camber angle on the design results also need to be clarified.

In this paper, an aerodynamic design method for a CROR based on lifting line theory is presented. The solidity and camber angle were varied by changing the number of blades. Several aerodynamic designs were accomplished. Then, the differences in aerodynamic performance were analyzed and the correlation between the designed number of blades and solidity and camber angle was also obtained. A study on the effects of solidity and camber angle on the aerodynamic performance was then conducted. Finally, considering the above results, recommendations are provided for selecting the number of blades in aerodynamic design.

2. AERODYNAMIC DESIGN METHOD OF CROR

2.1 One-Dimensional Aerodynamic Design Method

The aerodynamic design of a CROR involves two steps. The first is a one-dimensional aerodynamic design process to obtain the radial distribution of parameters, including the inlet flow angle and airflow turning angle. The second is the three-dimensional modeling process to complete the modeling according to the radial distribution of the parameters.

For one-dimensional aerodynamic design, the design model of the CROR rotor was constructed based on the lifting line theory. Each blade of the rotor was replaced by a lifting line. Two lifting lines were selected during the design process. These were discretized into *m* segments along the radial direction, each with an attached horseshoe vortex.

Similar to the propeller, the CROR was affected by the induced velocities. Those generated by the front and rear rotors must be considered because both are capable of generating induced velocities in the flow field. For each blade, the induced velocity includes not only the induced velocity on itself but also the inter-induced velocity between the rotors. The induced velocity is related to the blade load and the induced velocity factor. Calculation of the induced velocity factor can be carried out using the Biot-Savart law, which is related to the relative position between the control points, the inlet flow angle, and the rotor spacing. The numerical solution of the induced velocity based on the vortex lattice model can be used to solve the self-induced and inter-induced velocities at the segments. The velocity triangle for a CROR is given in Fig. 1. where $w_{1,f}$ is the relative velocity of the front inlet flow; $w_{1a,f}$ and $w_{1t,f}$ are the axial and circumferential relative velocity at the front inlet, respectively; $w_{2,f}$ is the front outlet relative velocity. $c_{1,f}$ and $c_{2,f}$ are the absolute velocities at inlet and outlet, respectively; $\Delta\beta_f$ is the turning angle of the front airflow; and ω_f and ω_r are the rotational speeds of the rotors. The rear rotor's velocity triangles are similar and differentiated using the subscript r. Owing to the small axial spacing of the CROR, the front outlet absolute velocity can be considered approximately equal to the rear inlet absolute velocity:

$$c_{2,f} = c_{1,r} \tag{1}$$

According to the velocity triangle, the thrust generated by the front rotor (FR) is:

$$T_f = \rho Z_f \sum_{m=1}^{M} w_{1t,f}(m)\Gamma_f(m)\Delta l_f - D_f \tag{2}$$

The torque required for the FR is

$$Q_f = \rho Z_f \sum_{m=1}^{M} w_{1a,f}\Gamma_f(m) r_{c,f}(m)\Delta l_f \tag{3}$$

where ρ is the density, Z_f is the number of blades, Γ_f is circulation of the lifting line segment, Δl_f is the length of the lifting line segment, and D_f is the hub resistance.

The thrust and torque of the rear rotor (RR) were calculated in the same way. During the design process, the following conditions should be satisfied:

$$Q_r = Q_f \tag{4}$$

$$T_{\mathrm{f}} + T_{\mathrm{r}} = T_{\mathrm{required}} \tag{5}$$

where T_{required} is the required thrust. The aerodynamic design problem for a CROR can be summarized as solving for the load distribution that minimizes the shaft power under a thrust requirement.

The Lagrange multiplier method is introduced to solve the circulation distribution that minimizes the shaft power while satisfying the thrust requirement. The following auxiliary equations are established according to the Lagrange multiplier method:

$$\begin{aligned} H = &\left(\omega_{\mathrm{f}} Q_{\mathrm{f}} + \omega_{\mathrm{r}} Q_{\mathrm{r}}\right) + \lambda_T \left(T_{\mathrm{f}} + T_{\mathrm{r}} - T_{\mathrm{required}}\right) \\ &+ \lambda_Q \left(\mathrm{Q}_{\mathrm{r}} - Q_{\mathrm{f}}\right) \end{aligned} \tag{6}$$

where λ_T and λ_Q are the Lagrange multipliers. To solve for the optimal circulation distribution, the following must be satisfied:

$$\frac{\partial H}{\partial \Gamma_{\mathrm{f}}(i)} = 0 \tag{7}$$

$$\frac{\partial H}{\partial \Gamma_{\mathrm{r}}(i)} = 0 \tag{8}$$

$$\frac{\partial H}{\partial \lambda_T} = \mathrm{T}_{\mathrm{f}} + \mathrm{T}_{\mathrm{r}} - T_{\mathrm{required}} = 0 \tag{9}$$

$$\frac{\partial H}{\partial \lambda_Q} = Q_{\mathrm{f}} - Q_{\mathrm{r}} = 0 \tag{10}$$

Equations (7)-(10) are the control equations for the one-dimensional aerodynamic design of the CROR.

2.2 Effect of Front Rotor Wake on Rear Rotor

The RR works in the front wake; thus, the inlet velocity of the RR was influenced by the operating conditions of the FR. In the one-dimensional aerodynamic design process, the connection between the rotors should be considered. The velocity of the front rotor's wake was calculated by the load and inlet velocity of the FR.

According to the velocity triangle in Fig. 1, the circumferential relative velocity at the front outlet can be expressed as:

$$w_{2\mathrm{t,f}} = w_{1\mathrm{t,f}} - \Delta w_{\mathrm{t,f}} \tag{11}$$

According to the definition of circulation, the difference between the relative velocities of the front inlet and outlet flows in the circumferential direction is

$$\Delta w_{\mathrm{t,f}} = \Gamma_{\mathrm{f}} / t \tag{12}$$

where t is the blade pitch. The compressibility of the flow cannot be neglected because of the high flight Mach number. The flow state in the channel was similar to that of a fan and compressor. Significant shock waves were observed in the channel. The axial relative velocity at the front outlet is no longer equal that at the front inlet.

According to the propeller's actuator disk model, the propeller can be regarded as a disk with infinite blades. This plane caused a sudden pressure increase. The disk generates thrust through this pressurization process (Farrar& Agarwal, 2015). This study adopted the actuator disk model. A normal shock is used to simulate the pressurization of the FR to carry out a simple calculation of the relationship between the axial velocities at the front inlet and outlet. According to the momentum theory, the static pressure ratio of the front rotor can be expressed as

$$\pi_{\mathrm{f}} = 1 + T_{\mathrm{f}} / \left(A_{\mathrm{f}}\, p_0\right) \tag{13}$$

where A_{f} is the annular area of the FR, and p_0 is the ambient static pressure. After obtaining the static pressure ratio, the ratio of the axial velocity at the inlet and outlet was obtained according to the relationship between the velocity ratio and pressure ratio before and after the normal shock.

Then the axial velocity at the front outlet can be obtained. Combined with the circumferential component of the relative velocity at the front outlet, the wake velocity of the FR was obtained.

2.3 Three-Dimensional Modeling Method

The velocity over the entire field and the radial distribution of the circulation are obtained by one-dimensional aerodynamic design. To perform the modeling of the CROR, the two-dimensional cross-section modeling was first completed based on the radial distribution of parameters. Then, a stacking line was introduced to complete the three-dimensional modeling.

The three-dimensional modeling process is shown in Fig. 2. The cross-sectional modeling parameters used include the camber angle, maximum camber position, chord length, and stagger angle.

In this study, a two-dimensional cross-section was constructed by applying the NACA0016 profile with a double-circular-arc camber line. The camber angle was determined from airflow turning angle obtained in the one-dimensional aerodynamic design as well as the deviation angle calculated by the modified Carter's formula (Cetin et al.,1987).

The stagger angle was determined by the inlet airflow angle and angle of attack, which were selected as 0°. The $\tilde{f}$ was the same as the maximum thickness position of the NACA0016 airfoil. The chord length had less influence on the thrust, and a distribution similar to that of F7A7 was used (Hoff, et al.1990).

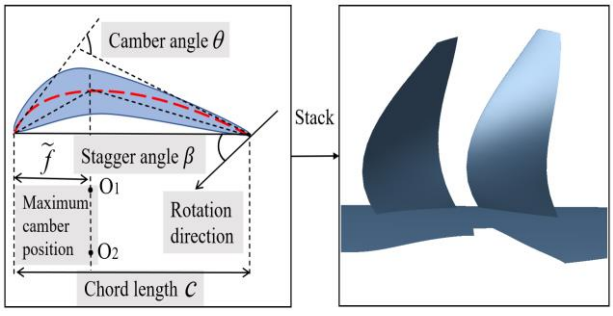

Fig. 2 Process of building the CROR geometry

3. NUMERICAL METHOD AND VALIDATION

3.1 Numerical Simulation Methods

The numerical simulation was performed using the commercial software *Numeca*. The Spalart-Allmaras model was the turbulence model, and an ideal gas was used for the numerical calculations. Considering the flow characteristics of the CROR and consumption of computational resources, a single channel was selected for the calculation. The hub was simplified into an infinite-length cylindrical surface.

A rotating CROR can affect its surroundings, particularly in the radial direction. Therefore, when performing numerical simulations of the CROR, the size of the computational region must be selected considering the range of rotor disturbances. Combined with the previous studies on the influence range of the CROR (Zachariadis & Hall, 2011; Stuermer, 2008), the distance of the front boundary from the front rotor was 8*R*. *R* is the rotor radius. The distance of the rear boundary from the rear rotor was 8*R*. The radius of the radial far-field boundary was 6*R*.

Pressure inlet boundary conditions were used for the front and radial far-field boundaries, nonreflective boundary conditions were used for the rear boundary. The circumferential boundary is a periodic boundary condition. The entire computational domain was divided into two with different rotational speeds. The boundary conditions of the domain interface used a mixed plane. A summary of the computational domain and boundary conditions are shown in Fig. 3(a).

The grids were generated using *AutoGrid5*, the details of which are shown in Fig. 3(b). The grid consists of an O-type mesh around the blade and an H-type mesh in the channel. The height of the first layer of the grid was 1×10^{-5}m and the y-plus was less than 10.

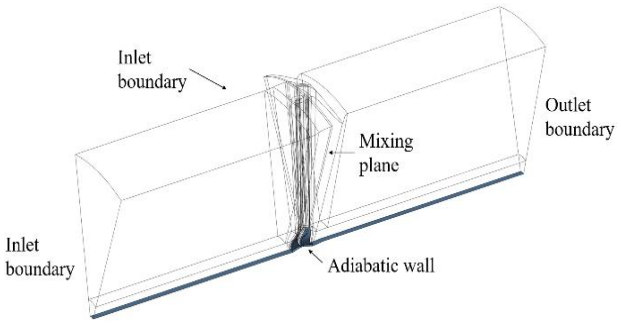

(a) Boundary conditions for numerical simulation

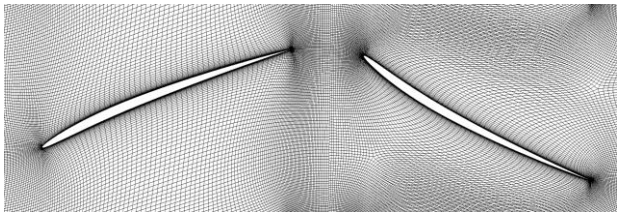

(b) Calculation grids

Fig. 3 Numerical simulation method for CROR

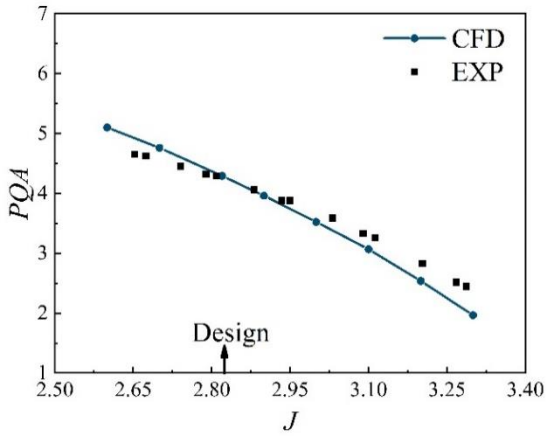

(a) Comparison result of the total power coefficient

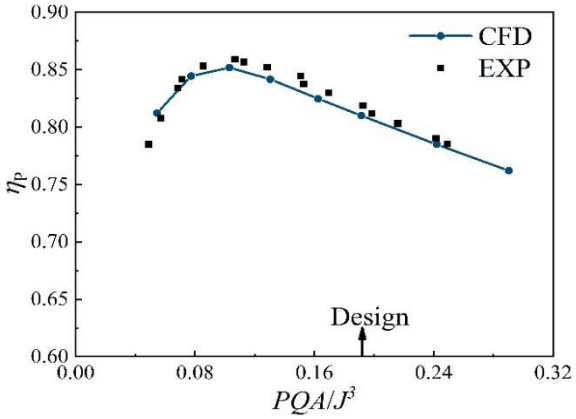

(b) Comparison result of the propulsion efficiency

Fig. 4 Comparison of experiment and CFD results

3.2 Validation of the Numerical Simulations

The numerical simulation method was validated using the F7A7 scaled model from reference (GE36 Design and Systems Engineering, 1987; Hoff, et al., 1990). The flight Mach number is 0.72. The designed advance ratio is 2.8. The advance ratio is defined as

$$J = \frac{v_s}{nD} \tag{14}$$

where v_s is the speed, n is the rotational speed, and D is the diameter. A comparison of the experimental and computational fluid dynamics (CFD) results is shown in Fig. 4. The parameters used for the comparison include the total power coefficient, propulsion efficiency, and torque ratio. The total power coefficient for the CROR is calculated as

$$PQA = \frac{P}{A\rho n^3 D^3} \tag{15}$$

where P is the power of the CROR, A is the annular area of the channel, and ρ is the density. The power of the CROR includes the power of the both rotors.

$$P = \omega_f \cdot Q_f + \omega_r \cdot Q_r \tag{16}$$

The propulsion efficiency of the CROR is defined as:

$$\eta_{\mathrm{P}}=\frac{v_S \cdot T}{P} \tag{17}$$

where T is the thrust, which is the axial component of the sum of the pressure and viscous forces on the blade surface.

A comparison of the total power coefficient under different advance ratios is shown in Fig. 4(a). The total power coefficients obtained from the CFD at the design point, i.e., when the advance ratio is 2.8, agree well with the experimental results. At the off-design point, the trend of the total power coefficient obtained from the numerical simulation was similar to that obtained from the experiment. At the advance ratio, which is far from the design point, there is a difference between the overall performance obtained by the CFD and experiment, possibly because of the different levels of blade deformation. A comparison of the experimental and numerical simulation results in the reference (Zachariadis & Hall, 2011) also revealed this difference.

Figure 4(b) shows a comparison of the propulsion efficiency under different advance ratios. The trends obtained from the numerical simulations agreed well with the experimental results, and the prediction of the peak efficiency point was accurate.

In summary, the numerical simulation method used in this paper can simulate the aerodynamic performance of a CROR.

3.3 Grid Independence Study

To estimate the effect of grid quantity on the computational results, a grid-independence study was conducted. Three sets of grids with different grid quantities are computed: 2.9 million, 5.2 million, and 8.5 million for coarse, medium, and fine grids, respectively.

The calculated thrust and power coefficients obtained from the three sets of grids and their relative errors are listed in Table 1. The thrust and power coefficients are defined as

$$C_T=\frac{T}{\rho n^2 D^4} \tag{18}$$

$$C_P=\frac{P}{\rho n^3 D^5} \tag{19}$$

For the thrust coefficient, the relative error between the coarse and medium grids is 0.431%. For the power coefficient, the relative error between the coarse and medium grids is 0.530%. Comparing the thrust and power coefficients obtained from the medium and fine grids, the relative errors were smaller.

Table 1 Grid Independence

	Coarse	Medium	Fine
Thrust coefficient	1.1011	1.0964	1.0962
Power coefficient	4.7519	4.7269	4.7264
Relative error of thrust coefficient	0.431%	0.016%	
Relative error of power coefficient	0.530%	0.010%	

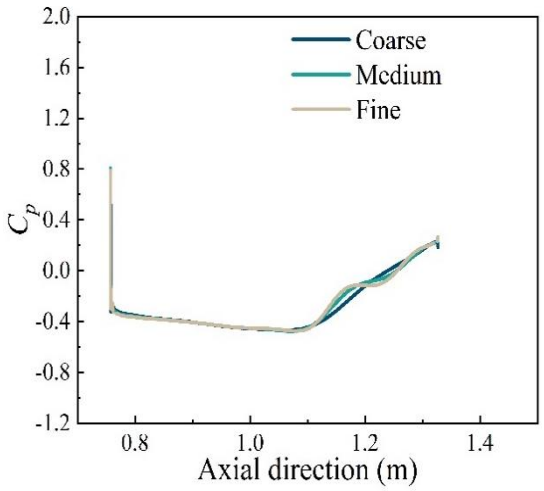

Fig. 5 Static pressure distribution on blade suction surface with different grid numbers

A comparison of the calculated pressure coefficients on the suction surface with different grid quantities is given in Fig. 5. The static pressure coefficient is defined as

$$C_p=\frac{p-p_0}{\frac{1}{2}\rho_\infty {v_\infty}^2} \tag{20}$$

where p is the static pressure. The coarse grid captured the pressure variations poorly, while the medium and fine grid calculation results were close to each other and captured the pressure variations more accurately.

Considering the computational accuracy and consumption of computational resources, a grid of 5.2 million was selected for the numerical simulation in this study.

4. EFFECT OF SOLIDITY AND CAMBER ANGLE ON AERODYNAMIC PERFORMANCE

4.1 Requirements for CROR Design

When using the previously described aerodynamic design methods for the CROR, the design parameters include the front and rear rotors' rotational speed, diameter, hub ratio, rotor spacing, and required thrust. In this study, the aerodynamic design of a CROR was performed under cruise conditions. When performing the design in this section, only the number of blades is changed; the remaining design parameters remain unchanged, and the required thrust coefficient is 1.091. Referring to the number of blades of the existing CROR, such as the F31A31 with 12 front blades and 10 rear blades, AI-PX7 with 11 front blades and 9 rear blades, Rig-140 with 7 front blades and 7 rear blades (Kirker, 1990; Wojno & Janardan, 2013; Falissard et al., 2018;), this study used five sets of designs with 6, 8, 10, 12, and 14 blades, respectively.

Except for the number of blades, all other design parameters of these five designs are the same. The detailed design parameters are listed in Table 2.

Table 2 Design parameters of the CROR

	Parameters	Values
Design requirements	Flight altitude(m)	10668
	Mach number	0.785
	Required thrust coefficient	1.091±2%
Front rotor	Rotational speed	1000
	Diameter(m)	4
	Tip circular velocity (m/s)	209
	Hub ratio	0.4
Rear rotor	Rotational speed	1000
	Diameter(m)	4
	Tip circular velocity (m/s)	209
	Hub ratio	0.4
	Spacing(m)	0.9

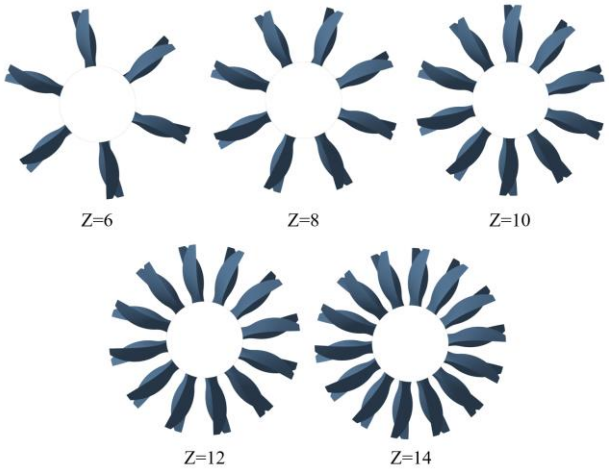

(a) Front view

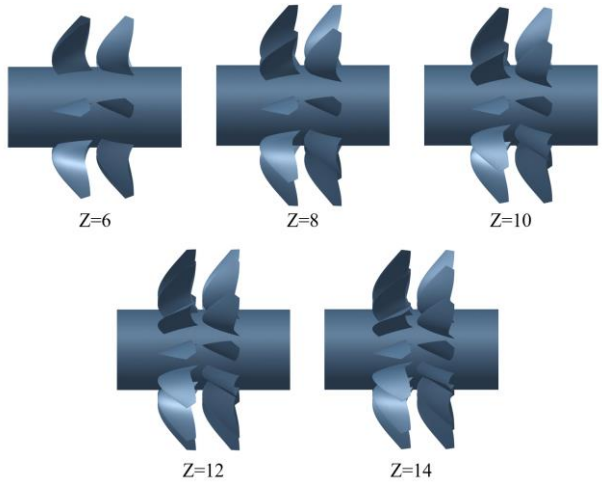

(b) Side view

Fig. 6 The geometry of the designed CRORs

4.2 Differences in Solidity and Camber Angle

Five different sets of aerodynamic designs were created using different numbers of blades. The geometries of the CROR obtained from the designs are shown in Fig. 6.

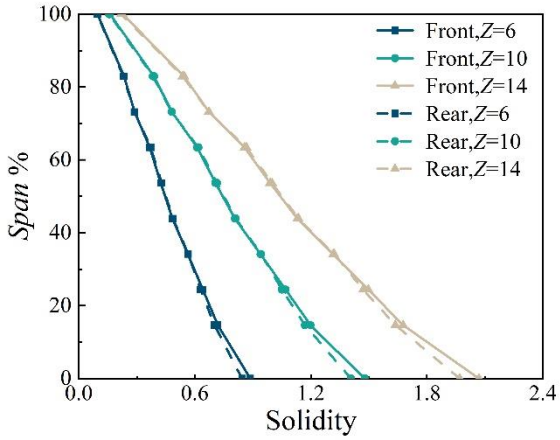

(a) Radial distribution of solidity with different design blade numbers

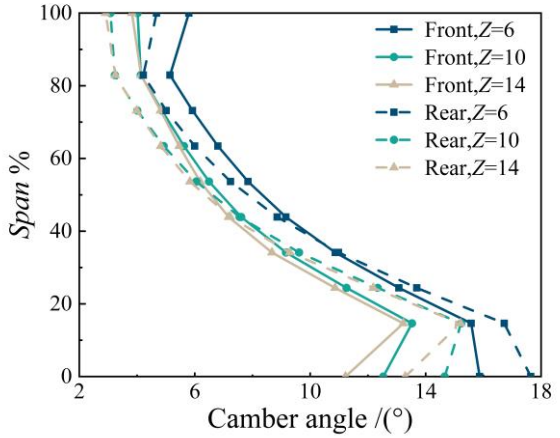

(b) Radial distribution of camber angle with different design blade numbers

Fig. 7 Radial distribution of solidity and camber angle with different design blade numbers

Using different blade numbers, the designed CROR exhibited significant differences in the solidity and camber angle. The solidity is the ratio of the chord length to the blade pitch (spacing).

$$\tau = \frac{b}{t} \tag{21}$$

Figure 7 shows the solidity and camber angle for different numbers of blades. It can be found that the solidity is positively related to the number of blades because the chord length is approximately constant, while the blade pitch is inversely related to the number of blades. For an open rotor with 10 blades, the solidity from the root to top ranges between 1.5 and 0.15. Owing to the small number of blades in the open rotor, the change in solidity was greater when the number of blades was changed. For example, at 50% blade height, the front blade solidity for the three open rotors is 0.70, 1.17, and 1.64.

Figure 7(b) shows that the increased blades have a tendency to decrease the camber angle. However, this

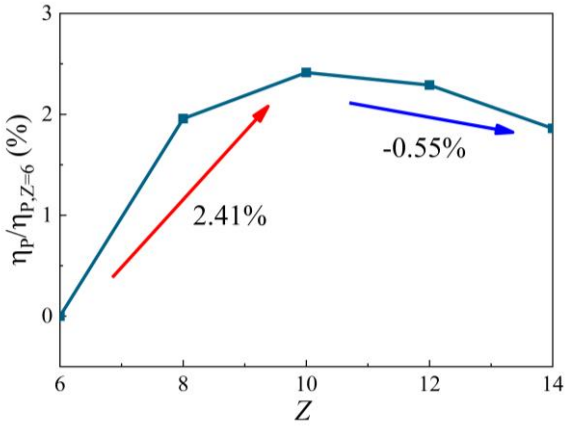

Fig. 8 Propulsion efficiency of CRORs with different blade numbers

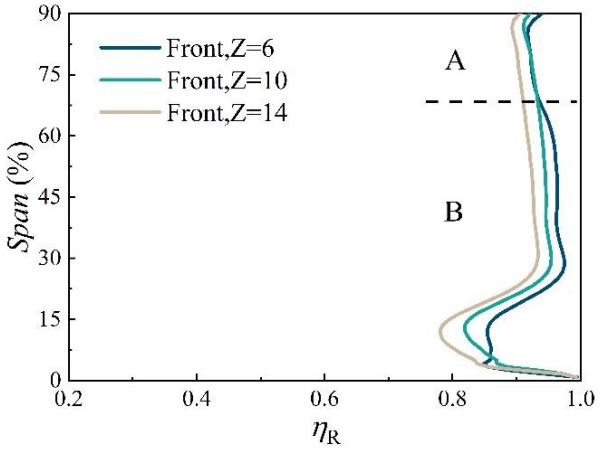

(a) Front rotor

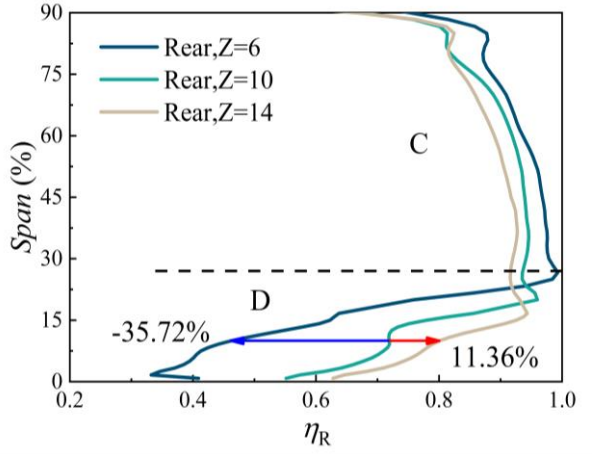

(b) Rear rotor

Fig. 9 Radial distribution of isentropic efficiency of CRORs

change is nonlinear; for example, the camber angle at 50% blade height of the front rotor is 8.34°, 6.92°, and 6.56° for the three open rotors. Taking the front rotor as an example, the reason is that when the designed blade number changes while the other design parameters remain unchanged, the circulation Γ_f and blade number Z should be approximately inversely proportional, as shown in Eq. (2). The blade pitch t is also inversely proportional to the blade number Z, as shown in Eq. (12). $\Delta w_{t,f}$ is the ratio of Γ_f and t; thus, $\Delta w_{t,f}$ should be approximately constant.

Because the rotation speed is constant, $w_{1t,f}$ is constant; thus, $\Delta w_{t,f}/w_{1t,f}$ is also constant. Therefore, the airflow turning angle remained unchanged when Z changes. However, when the blades increase, the solidity increases and the deviation angle decreases. The corresponding camber angle decreases, but this change is smaller. Therefore, the camber angle was changed due to the change in the deviation angle caused by the change in solidity.

4.3 Differences in Aerodynamic Performance

The numerical simulation of these five designs was performed. The variation trend of the overall propulsion efficiency is shown in Fig. 8. There exists an optimal Z in aerodynamic design. When the number of blades increase, the overall propulsion efficiency first increases and then decreases. The highest overall propulsion efficiency was 0.81 when the number of blades was 10. The lowest overall propulsion efficiency occurred when the number of blades was six. The highest value was 2.41% higher than the lowest value. When the number of blades was 14, the total propulsion efficiency decreased by 0.55%. It is worth noting that the reduction in propulsion efficiency caused by too few blades was much larger than that caused by too many blades.

Figure 9 shows the radial distribution of the isentropic efficiency. The isentropic efficiency at each radial position is

$$\eta_R = \frac{\left(P^*_{out}/P^*_{in}\right)^{\frac{\gamma-1}{\gamma}} - 1}{\left(T^*_{out}/T^*_{in}\right) - 1} \tag{22}$$

where γ is the gas constant. The front rotor can be divided into two regions, A and B, with 68% blade height as the boundary. In region B, the distribution features of the isentropic efficiency with different blade numbers were similar, with fewer blades resulting in a higher isentropic efficiency. In region A, the isentropic efficiency of the rotor with fewer blades exhibited a downward trend because of the large camber angle and circular velocity at the tip.

For the rear rotor, there were obvious differences in the isentropic efficiency distribution with different blade numbers. It can also be divided into C and D regions at 27% blade height. In region C, fewer blades resulted in higher isentropic efficiency, which is consistent with the phenomenon in region B. In region D, the isentropic efficiency of the rotor with fewer blades was significantly reduced. At 10% blade height, the isentropic efficiency of the CROR with six blades was reduced by 35.72% compared with that with 10 blades. In contrast, the CROR with 14 blades had an 11.36% higher isentropic efficiency. This can also explain the sudden decrease in the propulsion efficiency when the number of blades is 6, as shown in Fig. 8.

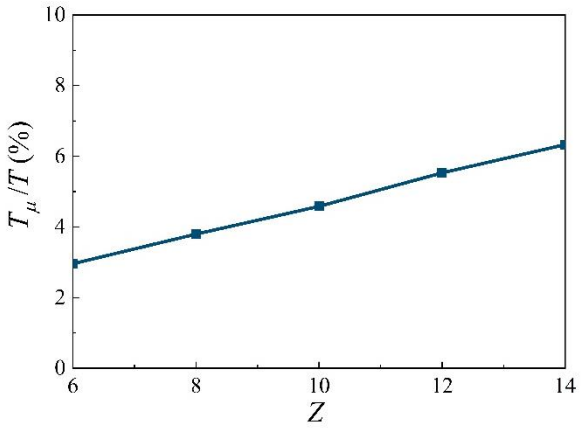

Fig. 10 Proportion of viscous force with different design blade numbers

4.4 Effect of Solidity and Camber Angle

The blade surface is primarily stressed by viscous and pressure forces; therefore, the axial thrust received by the rotors can be expressed as the difference between the pressure and viscous forces in the axial direction:

$$T = T_P - T_\mu \tag{23}$$

where T_P is the axial pressure force and T_μ is the axial viscous force. When the number of blades and solidity increased, the overall viscous force changed significantly. The overall thrust remained constant during the design process. To quantitatively analyze the effect of viscous forces when the solidity changes, the proportion of viscous forces with different number of blades is shown in Fig. 10.

It can be observed that the viscous force is proportional to the number of blades. This is primarily because the viscous force is related to the surface area and velocity distribution. When the speed and thrust remain unchanged, the velocity field of the CRORs with different blade numbers was approximately the same, while the surface area was proportional to the *Z*; the viscous force was proportional to the *Z*.

With 6 blades, the proportion of viscous force was 2.96%, that is, T_P/T was 102.96%. With 14 blades, the proportion of viscous force was 6.33%, that is, T_P/T was 106.33%. For the point with the highest propulsion efficiency, that is, when there are 10 blades, the proportion of viscous force was 4.58%. Even if the designed number of blades reached 14, T_P/T_μ is 16.80. The axial pressure force is much larger than the axial viscous force. This indicates that when the number of blades increase significantly, as long as the overall thrust required for the design remains unchanged, the total pressure force changes less.

When the solidity changed, the features of the wake also changed. Figure 11 gives the absolute total pressure at the outlet. The positions of the suction surface (SS) and pressure surface (PS) are marked in the figure. When the solidity increased, the low total pressure area caused by the wake area expanded. In addition, the CROR with fewer

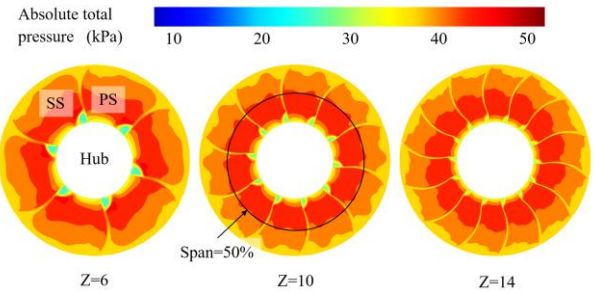

Fig. 11 Absolute total pressure distribution at the rear rotor outlet

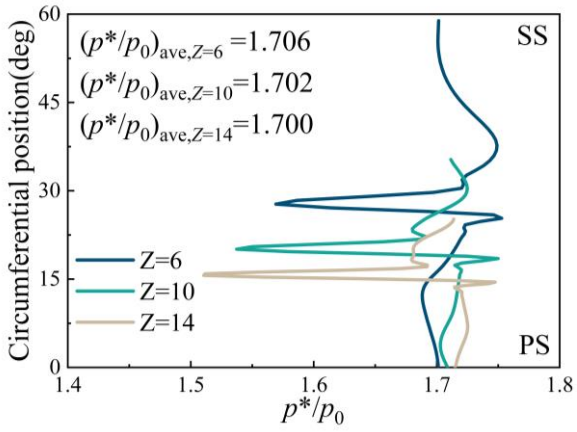

Fig. 12 Absolute total pressure distribution at different circumferential positions within a single channel at 50% blade height

blades had a significantly smaller low total pressure region at the root position. This is similar to the isentropic efficiency distribution shown in Fig .9.

Figure 12 shows the absolute total pressure (within a single blade channel) at the outlet at different circumferential positions at 50% blade height. A low total pressure region exists for all three designs owing to the wake. However, the low total pressure region was wider owing to the larger camber angle for the design with fewer blades, while the low total pressure region was narrower for the CROR with a larger blade number. The mean total pressure in a single channel was very close to each other because of the same thrust requirement for all three CRORs. However, the presence of the wake lowers the mean total pressure for the CROR with more blades. This explains the decrease in the isentropic efficiency of the design with more blades in regions B and C, as shown in Fig. 9.

The relative Mach number at the inlet of the rotors are shown in Fig. 13. When the number of blades is changed, the changes in inlet parameters of the rotors are small for different blade numbers because it ensures that the required thrust remains the same. Comparing the relative Mach numbers at the front and rear inlets, the rear rotor has a higher inlet relative Mach number. In addition, the rear inlet relative Mach number was greater than 1 for most of the blade height ranges.

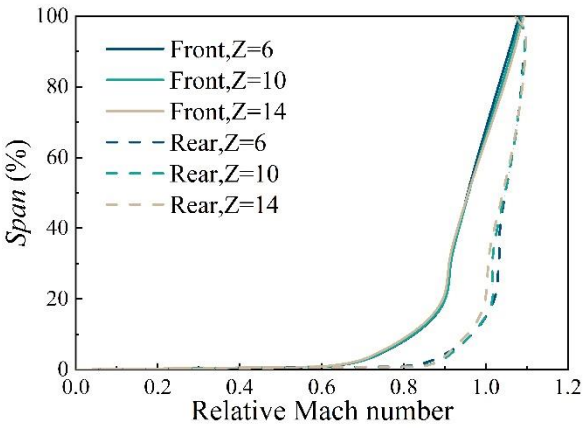

Fig. 13 Radial distribution of relative Mach number at the front and rear inlet with different design blade numbers

For the CROR, the rotors are in the transonic incoming flow, hence there are certainly shock waves in the channel. When the designed blade number is changed, the change in the solidity will have an effect on the shock wave structure. The contours of the relative Mach number at different blade heights with different blade numbers are shown in Fig. 14.

For an isolated airfoil, such as a wing, in the face of highly subsonic incoming flow, it will generate a detached shock wave at the leading edge (LE) and recompression shock wave at the trailing edge (TE) (Liu et al., 2019). For the CROR with six blades, the flow at 50% blade height was similar to that of the wing. A detached and recompression shock wave can be observed at the LE and TE, respectively. The detached and recompression shock waves of the two neighboring blades almost overlapped in one place.

As the designed blade number increased, the pitch between the two blades decreased, the solidity increased, and the relative positions of the detached and recompression shock waves deviated. The detached shock wave intruded into the blade channel while the recompression shock wave transformed into a passage shock wave.

When the designed blade number was 14, the two shockwaves were completely separated. The detached shock wave remained because the high relative Mach number of the inlet extended to the SS of the neighboring blade. The distance between the detached and passage shock waves increased. The shock wave structure at this point was similar to that in a compressor (Boyer & O'Brien, 2003).

The change of shock wave structure led to the change of the static pressure distribution. The static pressure distribution at different blade heights for the rear rotor are shown in Fig. 15.

By comparing the cross-sectional static pressure distributions of the CRORs with different blade numbers, two features can be identified. The first is the pressure difference between the SS and PS of the CROR with fewer blades is greater because the same thrust is guaranteed; the fewer the blades, the higher the individual blade load. The second is that when six blades are used, the SS pressure change characteristics are very different from those of the other two blades, which is mainly due to the different shock wave structures. At 50% blade height, the pressure on the SS increases to the outlet pressure over a short axial distance, which is similar to the propeller (Boulkeraa et al., 2022). These two features result in the flow having a greater inverse pressure gradient in the flow direction near the TE of the SS when the number of blades is small.

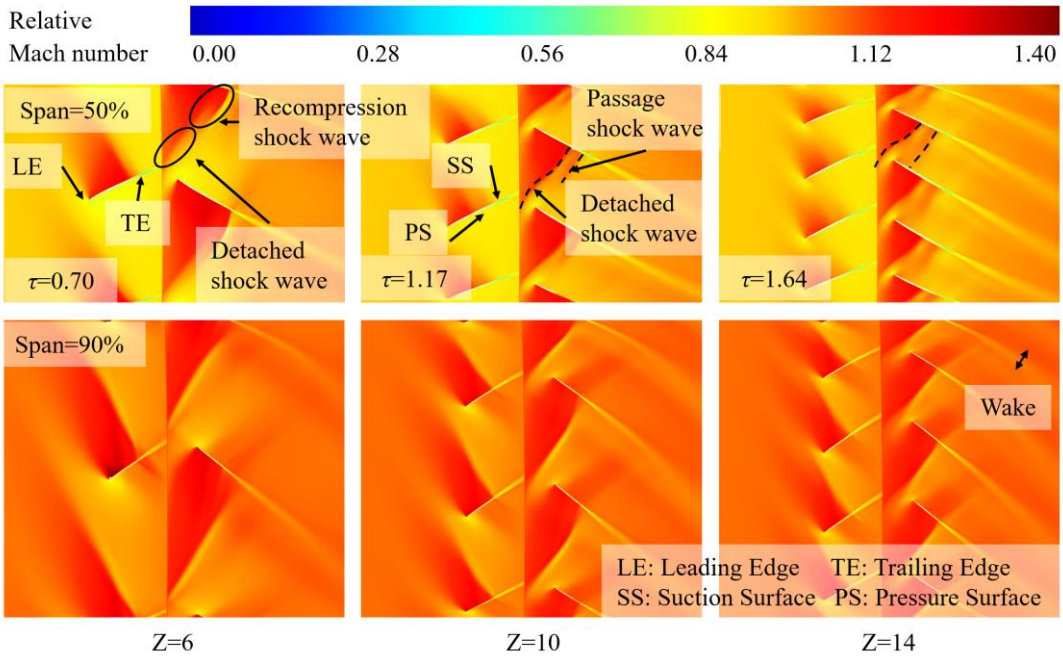

Fig. 14 Contour of relative Mach numbers at different blade heights with different blade numbers

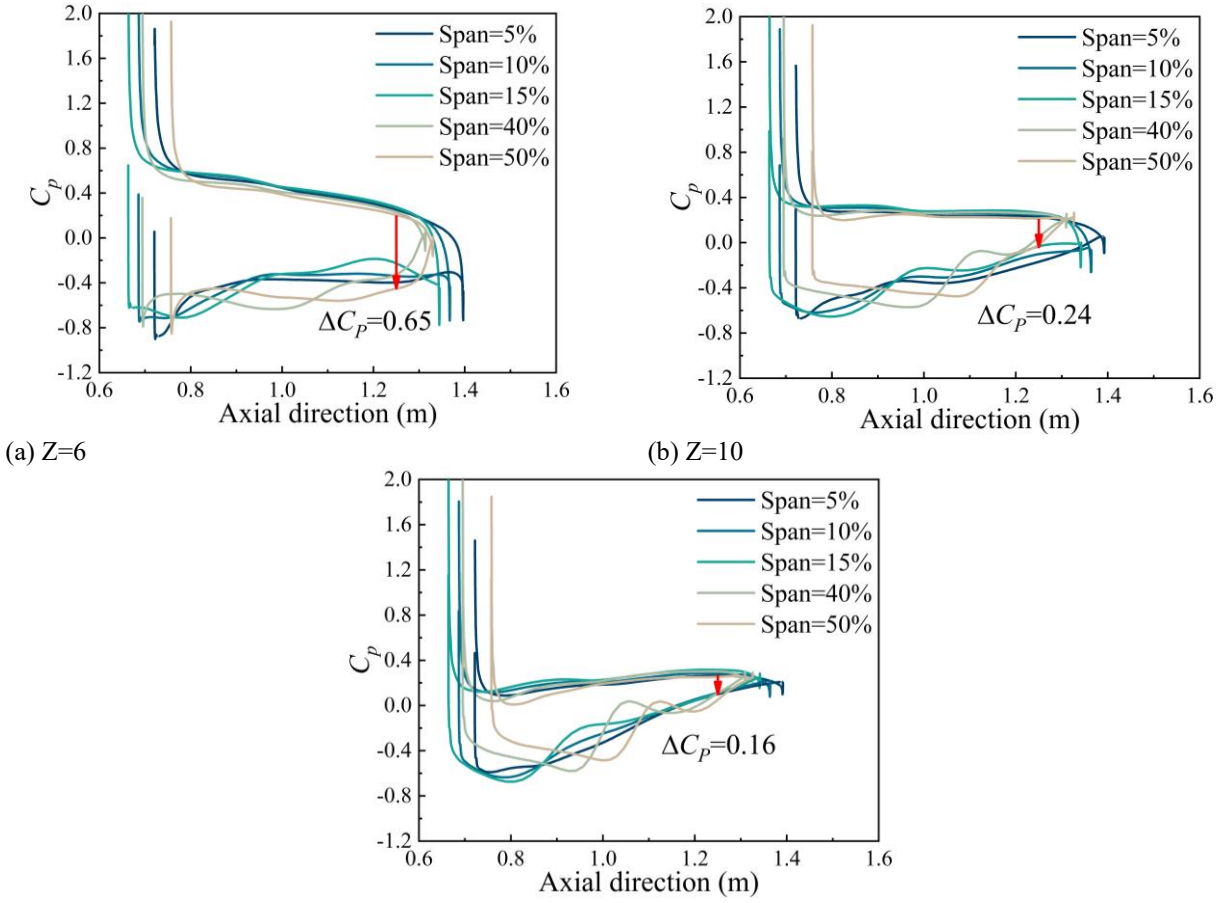

(a) Z=6 (b) Z=10

(c) Z=14

Fig. 15 Rear blade surface static pressure distribution with different blade numbers

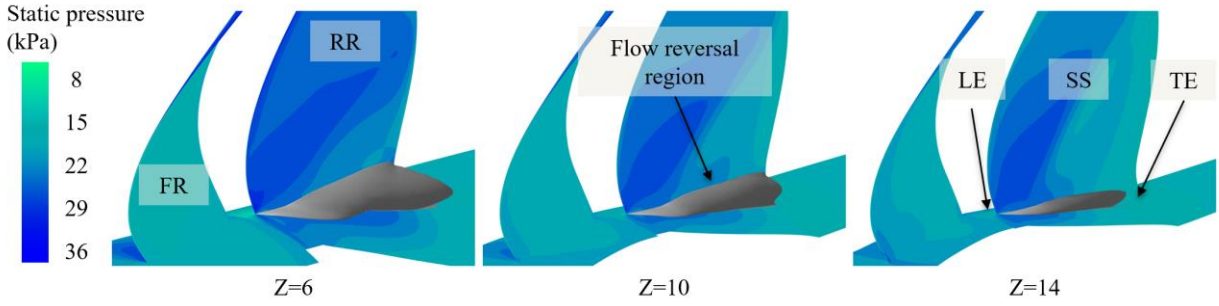

Fig. 16 Flow reversal region inside the blade channel

As the blades decreased, the camber angle increased, and the pressure difference between the SS and PS increased. Owing to the change in the shock wave structure, this pressure difference near the TE is further increased. This results in a larger pressure difference near the TE for designs with fewer blades.

The red arrow in the figure indicates the difference in pressure coefficients at the same axial position at 50% blade height. The pressure difference was significantly greater with fewer blades. This feature was observed for other blade height positions. This pressure difference between the suction and pressure surfaces also indicates a large pressure difference between the two neighboring blades. Eventually, this resulted in a large circumferential pressure difference near the channel outlet.

The above analysis illustrates that the camber angle increases while the solidity decreases significantly when the design has fewer blades. The larger camber angle brings a larger reverse pressure gradient. Simultaneously, a lower solidity causes the shock wave structure to change, resulting in a larger circumferential pressure difference in the channel.

These two pressure differences caused the low-momentum fluids to accumulate towards the TE, interacting with the hub boundary layer, and creating a significant corner separation. A significant flow reversal region developed in the channel, as shown in Fig. 16. The flow-reversal region is represented by an iso-surface with zero axial velocity. This also explains the significant

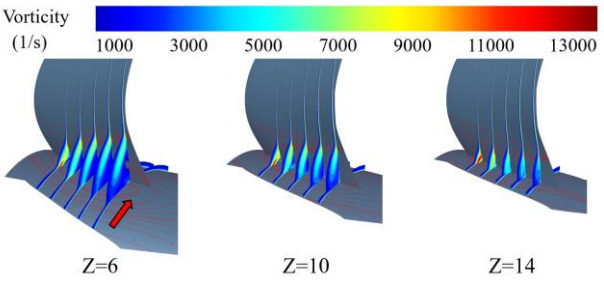

(a) Vortex features in blade channel

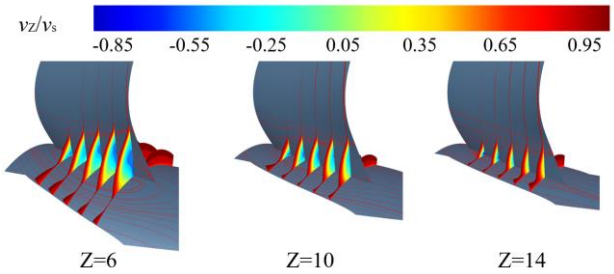

(b) Blockage in blade channel

Fig. 17 Vortex features and blockages due to the development of flow reversal regions

decrease in the isentropic efficiency at the root position when the rotor has 6 blades.

Such a severe corner separation led to more apparent vortex features at the root of the blade and caused blockage on the flow. Figure 17(a) shows that the circumferential pressure difference causes the limiting streamline on the hub to shift toward the SS. In Fig. 17(b), the actual flow area is reduced because of the blockage, making the flow velocity in the middle faster and the hub boundary layer thinner.

5. CONCLUSION

This paper presented an aerodynamic design method for a CROR based on lifting-line theory. By changing the number of blades, the solidity and camber angle of the design results are changed, and several different aerodynamic designs were completed. The effects of solidity and camber angle on the aerodynamic performance were studied. The detailed conclusions are as follows:

1. The aerodynamic design of the CROR was based on the required thrust. When the number of blades increased, the solidity increased, while the camber angle decreased. The solidity is positively related to the blade number. The change in the camber angle is nonlinear. The reason for this change comes primarily from the change in the deviation angle owing to the change in solidity. The camber angle increased rapidly with the decrease in the number of blades.

2. The overall propulsion efficiency first increased and then decreased as the number of blades increased. There exists an optimal designed blade number for aerodynamic design. For the thrust required in this study, the highest propulsion efficiency was 0.81 with 10 blades. The reduction in propulsion efficiency caused by too few blades is much greater than caused that by too many blades. The highest propulsion efficiency is 2.41 % higher than the lowest value.

3. Increased solidity leads to increased viscous and wake losses, resulting in increased losses in the middle. Simultaneously, the solidity's change also changed the shock wave structure in the blade channel and the distribution of the static pressure. Therefore, the pressure difference between the SS and PS near the TE was large when the solidity decreased. This also means that the circumferential pressure difference in the channel was greater near the outlet. In contrast, when the number of blades is reduced, the increased camber angle resulted in a larger inverse pressure gradient in the flow direction. Eventually, the pressure difference in the flow direction and circumferential pressure difference caused the fluid to accumulate toward the TE, interacting with the hub layer and leading to corner separation. A significant flow reversal region occurred at the root, resulting in flow losses.

4. When the designed CROR had fewer blades, the viscous and wake losses were smaller. However, they were more likely to result in corner separation at the rear root, leading to higher losses. At 10 % blade height, the isentropic efficiency of the CROR with 6 blades is reduced by 35.72 % compared to the CROR with 10 blades. When the designed CROR had more blades, the viscous and wake loss increased. Therefore, an optimum number of blades exists for the design. Furthermore, too few blades can cause more harm, and more blades should be used in the initial design. If the number of blades needs to be reduced, it is necessary to control the flow reversal region at the root.

ACKNOWLEDGEMENTS

The authors would like to express their gratitude for the financial support of the National Natural Science Foundation of China (No. 52076180), National Science and Technology Major Project (J2019- Ⅱ -0015-0036), Science Center for Gas Turbine Project (P2022-B-I-002-001, Funds for Distinguished Young Scholars of Shaanxi Province (2021JC-10), P2022-B- Ⅱ -010-001), and the Fundamental Research Funds for the Central Universities

CONFLICT OF INTEREST

The authors declare that they have no conflict of interest.

AUTHORS CONTRIBUTION

Qihang Wang: Conceptualization, Methodology, Validation, Formal analysis, Resources, Data curation, Writing—original draft, Writing—review & editing, Visualization; **Li Zhou**: Formal analysis, Resources, Writing—review & editing, Visualization, Supervision; **Zhanxue Wang**: Writing—review & editing, Supervision, Project administration.

REFERENCES

Aungier, R. H. (2003). *Axial-flow compressors: a strategy for aerodynamic design and analysis*. American Society of Mechanical Engineers, New York.

Barry, M., Sirvin, N.， & Boniface, J. (2014, July 28-30). *Open-rotor aerodynamics installation effects by a RANS-lifting line coupling method.* 50th AIAA/ASME/SAE/ASEE Joint Propulsion Conference, Cleveland, OH. https://doi.org/10.2514/6.2014-3887

Black, D. M., Menthe, R. W., & Wainauski, H. S. (1978). *Aerodynamic design and performance testing of an advanced 30 swept, eight bladed propeller at Mach numbers from 0.2 to 0.85.* NASA-CR-3047. Washington, D. C. : NASA.

Boyer, K. M., & O'Brien, W. F. (2003). An improved streamline curvature approach for off-design analysis of transonic axial compression systems. *Journal of Turbomachinery*, *125*(3), 475-481. https://doi.org/10.1115/1.1565085

Boulkeraa, T., Ghenaiet, A., & Benini, E. (2022). Optimum operating parameters and blade setting of a high-speed propeller. *Journal of Aircraft*, *59*(2), 484-501. https://doi.org/10.2514/1.C035861

Britsch, W. R., Osborn, W. M., & Laessig, M. R. (1979). *Effects of diffusion factor, aspect ratio and solidity on overall performance of 14 compressor middle stages.* NASA-TP-1523.

Brouckaert, J. F., Mirville, F., Phuah, K., & Taferner, P. (2018). Clean Sky research and demonstration programmes for next-generation aircraft engines. *The Aeronautical Journal*, *122*(1254), 1163-1175. https://doi.org/10.1017/aer.2018.37

Busch, G. R., Hassan, M., & Mavris, D. N. (2015, June 22-26). *Aircraft open rotor technology: analysis from an operational perspective*. 21st AIAA/CEAS Aeroacoustics Conference, Dallas, TX. https://doi.org/10.2514/6.2015-2359

Cetin, M., Ucer, A. S., & Hirsch, C. (1987). *Application of modified loss and deviation correlations to transonic axial compressors: AGARD-R-745.* Neuilly Sur Seine: NATO, 1987

Falissard, F., Boisard, R., Gaveriaux, R., Delattre, G., Gardarein, P., Chelius, A., & Mauffrey, Y. (2018). Influence of blade deformations on open-rotor low-speed and high-speed aerodynamics and aeroacoustics. *Journal of Aircraft*, *55*(6), 2267-2281. https://doi.org/10.2514/1.C034676

Farrar, B., & Agarwal, R. (2015). Computational fluid dynamics analysis of open-rotor engines using an actuator disk model. *Journal of Propulsion and Power*, *31*(3), 989-993. https://doi.org/10.2514/1.B35385

GE36 Design and Systems Engineering. (1987). *Full-scale technology demonstration of a modern counter rotating unducted fan engine concept-design report.* NASA-CR-180867. Washington, D. C.: NASA.

Hoff, G. E. (1990). *Experimental performance and acoustic investigation of modern, counterrotating blade concepts.* NASA-CR-185158. Washington, D. C. : NASA.

Hanson, D. B. (1983). Compressible helicoidal surface theory for propeller aerodynamics and noise. *AIAA Journal*, *21*(6), 881-889. https://doi.org/10.2514/3.60132

Kan, K., Chen, H., Zheng, Y., Zhou, D., Binama, M., & Dai, J. (2021a). Transient characteristics during power-off process in a shaft extension tubular pump by using a suitable numerical model. *Renewable Energy*, *164*, 109-121. https://doi.org/10.1016/j.renene.2020.09.001

Kan, K., Yang, Z., Lyu, P., Zheng, Y., & Shen, L. (2021b). Numerical study of turbulent flow past a rotating axial-flow pump based on a level-set immersed boundary method. *Renewable Energy*, *168*, 960-971. https://doi.org/10.1016/j.renene.2020.12.103

Kirker, T. (1990, October 22-24). *Procurement and testing of a 1/5 scale advanced counter rotating propfan model*. 13th Aeroacoustics Conference, Tallahassee, FL. https://doi.org/10.2514/6.1990-3975

Kuang, H., Wuli Chu, S., Zhang, H., & Ma, S. (2017). Flow mechanism for stall margin improvement via axial slot casing treatment on a transonic axial compressor. *Journal of Applied Fluid Mechanics*, *10*(2), 703-712. https://doi.org/10.18869/ACADPUB.JAFM.73.239.27047

Larsson, L., Lundbladh, A., & Grönstedt, T. (2014, June 16-20). *A conceptual design study of an open rotor powered regional aircraft*. Turbo Expo: Power for Land, Sea, and Air, Düsseldorf, Germany. GT2014-26091. https://doi.org/10.1115/GT2014-26091

Liu, Z., Liu, P., Qu, Q., & Hu, T. (2016). Effect of advance ratio and blade planform on the propeller performance of a high altitude airship. *Journal of Applied Fluid Mechanics*, *9*(6), 2993-3000. https://doi.org/10.29252/JAFM.09.06.25203

Liu, F., Han, Z. H., Zhang, Y., Song, K., Song, W. P., Gui, F., & Tang, J. B. (2019). Surrogate-based aerodynamic shape optimization of hypersonic flows considering transonic performance. *Aerospace Science and Technology*, *93*, 105345. https://doi.org/10.1016/j.ast.2019.105345

Nigam, N., Tyagi, A., Chen, P., Alonso, J. J., Palacios, F., Ol, M. V., & Byrnes, J. (2015, January 5-9). *Multi-fidelity multi-disciplinary propeller/rotor analysis and design*. 53rd AIAA Aerospace Sciences Meeting, Kissimmee, Florida. https://doi.org/10.2514/6.2015-0029

Perullo, C. A., Tai, J. C., & Mavris, D. N. (2013). Effects of advanced engine technology on open rotor cycle selection and performance. *Journal of Engineering*

for Gas Turbines and Power, *135*(7), 071204. https://doi.org/10.1115/1.4024019

Playle, S. C., Korkan, K. D., & Von Lavante, E. (1986). A numerical method for the design and analysis of counter-rotating propellers. *Journal of Propulsion and Power*, *2*(1), 57-63. https://doi.org/10.2514/3.22845

Rohrbach, C. (1976, July 26-29). *A report on the aerodynamic design and wind tunnel test of a prop-fan model*. 12th Propulsion Conference, Palo Alto, CA. https://doi.org/10.2514/6.1976-667

Smith Jr, L. H. (1987). Unducted fan aerodynamic design. *Journal of Turbomachinery*, *109*(3), 313-324 https://doi.org/10.1115/1.3262108

Stuermer, A. (2008, July21-23). *Unsteady CFD simulations of contra-rotating propeller propulsion systems*. 44th AIAA/ASME/SAE/ASEE Joint Propulsion Conference & Exhibit, Hartford, CT. https://doi.org/10.2514/6.2008-5218

Stürmer, A., Gutierrez, C. O. M., Roosenboom, E. W., Schröder, A., Geisler, R., Pallek, D., Agocs J., & Neitzke, K. P. (2012). Experimental and numerical investigation of a contra rotating open-rotor flowfield. *Journal of Aircraft*, *49*(6), 1868-1877. https://doi.org/10.2514/1.C031698

Sun, X., Meng, D., Liu, B., & Wang, Q. (2017). Numerical investigation of differential speed operation of two impellers of contra-rotating axial-flow fan. *Advances in Mechanical Engineering*, *9*(10), 1687814017720083. https://doi.org/10.1177/1687814017720083

Van Zante, D. E., Collier, F., Orton, A., Khalid, S. A., Wojno, J. P., & Wood, T. H. (2014). Progress in open rotor propulsors: The FAA/GE/NASA open rotor test campaign. *The Aeronautical Journal*, *118*(1208), 1181-1213. https://doi.org/10.1017/S0001924000009842

Wald, Q. R. (2006). The aerodynamics of propellers. *Progress in Aerospace Sciences*, *42*(2), 85-128. https://doi.org/10.1016/j.paerosci.2006.04.001

Wojno, J., & Janardan, B. (2013, May 27-29). *Comparison of NASA 9x15 low speed wind tunnel counter rotating open rotor data with GE-anechoic facility historic data for baseline F31A31 blade design*. 19th AIAA/CEAS Aeroacoustics Conference, Berlin, Germany. https://doi.org/10.2514/6.2013-2204

Zachariadis, A., & Hall, C. A. (2011). Application of a Navier-Stokes solver to the study of open rotor aerodynamics. *Journal of Turbomachinery*, *133*(3), 031025. https://doi.org/10.1115/1.4001246

Zhou Y. C., & Shan P. (2017). Inverse design approach for propfan aerodynamics based on compressible lifting surface theory. *Journal of Aerospace Power*, *32*(6), 1456-1469. https://doi.org/10.13224/j.cnki.jasp.2017.06.024